Dalton Transactions

Bismuth(III) - Thiophenedicarboxylates as Host Frameworks for Lanthanide Ions: Synthesis, Structural Characterization, and Photoluminescent Behavior

Journal:	*Dalton Transactions*
Manuscript ID	DT-ART-07-2018-002920.R1
Article Type:	Paper
Date Submitted by the Author:	16-Aug-2018
Complete List of Authors:	Adcock, Alyssa; Georgetown University, Department of Chemistry Gibbons, Bradley; Westminster College Einkauf, Jeffrey; Florida Atlantic University, Department of Chemistry Bertke, Jeffery; Georgetown University, Department of Chemistry Rubinson, Judith; Georgetown University, Department of Chemistry de Lill, Daniel; Florida Atlantic University, Chemistry and Biochemistry Knope, Karah; Georgetown University, Department of Chemistry

Bismuth(III) - Thiophenedicarboxylates as Host Frameworks for Lanthanide Ions: Synthesis, Structural Characterization, and Photoluminescent Behavior

Alyssa K. Adcock,[a] Bradley Gibbons,[b] Jeffrey D. Einkauf,[c] Jeffery A. Bertke,[a] J. Faye Rubinson,[a] Daniel T. de Lill,[c] and Karah E. Knope*[a]

[a]Department of Chemistry, Georgetown University, 37th and O Streets, NW, Washington, DC 20057
[b]Westminster College, 319 South Market Street, New Wilmington, PA 16172
[c]Department of Chemistry, Florida Atlantic University, 777 Glades Road, Boca Raton, FL 33431

Abstract

Three bismuth-2,5-thiophenedicarboxylates (Bi-TDC) and two europium-2,5-thiophenedicarboxylates (Eu-TDC) were synthesized under ambient conditions. The structures were determined through single crystal X-ray diffraction, and three of the phases were further characterized by powder X-ray diffraction, Raman spectroscopy, and thermogravimetric analysis. Reactions of bismuth nitrate, 2,5-thiophenedicarboxylate, and pyridine in an acidic solution of acetic acid and ethanol yield Hpy[Bi(TDC)$_2$(H$_2$O)]·1.5H$_2$O (**1**), whereas reactions in a water/ethanol mixture produce a minor phase, [Hpy]$_3$[Bi$_2$(TDC)$_4$(HTDC)(H$_2$O)]·0.74H$_2$O (**2**) along with a major product, (Hpy)$_2$[Bi(TDC)$_2$(HTDC)]·0.36H$_2$O (**3**). The structures of **1-3** are all built from anionic Bi-TDC chains that are further bridged through additional TDC linkages into interpenetrated 2D sheets. Addition of an aqueous lanthanide solution to the reaction mixtures of **1** and **2-3** resulted in the formation of doped phases, Hpy[Bi$_{1-x}$Ln$_x$(TDC)$_2$(H$_2$O)]·1.5H$_2$O (**Bi$_{1-x}$Ln$_x$-1**), where Ln=Nd, Sm, Eu, Tb, Dy, and Yb, and (Hpy)$_2$[Bi$_{0.99}$Eu$_{0.01}$(TDC)$_2$(HTDC)]·0.36H$_2$O (**Bi$_{0.99}$Eu$_{0.01}$-3**). Using europium nitrate rather than the bismuth precursor resulted in the formation of two homometallic europium based phases [Eu(TDC)(NO$_3$)(H$_2$O)]$_n$ (**4**) and [Eu$_2$(TDC)$_3$(H$_2$O)$_9$]·5H$_2$O (**5**), which adopt an extended 3D network and an interpenetrated 2D structure, respectively. Photophysical measurements were carried out for **1** and the lanthanide containing phases and quantum yield and lifetime values were determined for the visible light emitters. Herein, the structural chemistry, spectroscopic properties, and luminescence of the bismuth phases, their lanthanide doped analogs, and the europium compounds are presented.

Introduction

Due to their unique spectroscopic and magnetic properties, lanthanide-based materials have long been noted for their wide application in many high tech and energy related fields, commanding a great deal of research and development over the past several decades.[1-5] Their characteristic line-like visible and near-infrared emission allow several of the lanthanides (Ln) to be utilized in a variety of optical applications from display technologies to biomedical imaging to optical fibers.[2, 5-7] However, as the *f-f* transitions are Laporte forbidden, the Ln^{III} ions suffer from low molar absorptivities, wherein light absorption and thereby direct excitation is greatly inefficient.[8, 9] An "antenna" ligand with an excited state appropriately paired with the emissive manifold of the lanthanide ion is often utilized to sensitize the Ln^{III} ion thereby enhancing its photophysical properties. Additionally within inorganic phosphors, sensitizers/activators such as Bi^{3+}, UO_2^{2+}, or other Ln ions have been used to promote luminescence.[1, 10-13] Although Ln^{III} sensitization is well-known and for some systems including organic chromophores, heavily studied, there are emerging concerns regarding continued use of Ln-based materials, due to a lack of diverse global availability, high costs, and the heavy environmental impact of their separations and processing.[14] These considerations have prompted researchers to develop adequate luminescent alternatives and new classes of photoluminescent materials.[14]

Towards this end, our group has been targeting Bi-based materials and their Ln-doped analogs with the aim of developing novel photoluminescent materials. In recent years, bismuth and bismuth-based materials have attracted increasing attention due to the unique properties and environmentally-friendly attributes of Bi as well as the promising materials application of Bi based compounds to areas ranging from photocatalysis to pharmaceticals.[15-22] Yet, in contrast to d- and/or other p-block metals such as lead, there has been comparatively limited research with bismuth and relatively little work towards the development of Ln-doped Bi-organic compounds.[23-29] Examples of the latter include reports by Cheetham et al. employing 2,6-pyridinedicarboxylic acid and 1,4-benzenedicarboxylic acid to build Bi^{III} extended networks which incorporate 2 mol-% Eu and Tb into the host framework as well as the work by Müller-Buschbaum and coworkers that demonstrated the synthesis of 2D coordination polymers, $^2\infty[Bi_2Cl_6(pyz)_4]$, with subsequent Eu incorporation.[24-26] Stock and colleagues explored doping into eight bismuth(III)-tri- and tetracarboxlyates; however, successful incorporation of the Ln metal center was only observed for one of the phases utilizing pyromellitic acid.[27] Our group has also reported on Ln-doped Bi-organic materials, finding efficient emission from the europium doped phase.[28] At first glance, bismuth and the lanthanides make promising diadochic partners, with comparable ionic radii and a common trivalent oxidation state; however, significant synthetic challenges are prevalent in these systems due to differences in solubility and coordination geometry, often stemming from the presence of bismuth's stereochemically active lone pair.[30, 31] Furthermore, Bi-organic materials themselves have also been seen to exhibit unique luminescent properties, often stemming from ligand-to-metal or metal-to-ligand charge transfer, metal-based emission and/or ligand based emission.[24-27, 29, 31-39]

With the aim of capitalizing on both the established Ln sensitizing capabilities of 2,5-thiophenedicarboxylic acid (H_2TDC)[40-62] and/or the propensity of the bismuth metal center to enhance Ln luminescence coupled with the aforementioned similarities between Bi^{III} and Ln^{III}, in this work, we examined the room temperature synthesis of bismuth-based extended networks using H_2TDC and pyridine under aqueous conditions. Reported herein are the synthesis, structural characterization, and photoluminescent properties of three Bi-TDC compounds and the Ln-doped analogs of two of the phases. In an effort to draw comparisons between bismuth and lanthanide phases, reactions of europium and TDC under similar synthetic conditions were explored. The synthesis and characterization of these compounds is also reported.

Experimental Section

Materials

$Bi(NO_3)_3 \cdot 5H_2O$ (Fisher, 99.2%), $Eu(NO_3)_3 \cdot 6H_2O$ (BeanTown Chemical, 99.9%), $Ln(NO_3)_3 \cdot xH_2O$ (Ln = Nd, Sm, Tb, Dy, or Yb, x = 5 or 6, Strem Chemicals, 99.9%), 2,5-thiophenedicarboxylic acid (TCI, >98.0%), pyridine (Alfa Aesar, 99%), ethanol (Warner Graham Company), and glacial acetic acid (Fisher) were used as received. Nanopure water (≤0.05 μS; Millipore, USA) was used in all experiments.

Stock solutions. A 0.2 M solution of 2,5-thiophenedicarboxylic acid (H_2TDC) in ethanol, a 0.0267 M solution of bismuth nitrate pentahydrate in glacial acetic acid, and a 0.0267 M solution of europium nitrate pentahydrate in glacial acetic acid were prepared.

$Hpy[Bi(TDC)_2(H_2O)] \cdot 1.5H_2O$ (1)

An aliquot of a 0.0267 M solution of bismuth nitrate in glacial acetic acid (1.5 mL, 0.04 mmol), an aliquot of a 0.2 M solution of H_2TDC in ethanol (1.5 mL, 0.3 mmol), and pyridine (40 μL, 0.5 mmol) were loaded into a 10 mL glass vial ($pH_i \approx$ 4-5). An opaque, white suspension was initially observed upon addition of the reactants. The vial was capped and left on the benchtop at room temperature. After five to seven days, crystallization was observed ($pH_f \approx$ 5-6). The products were filtered, washed in water and ethanol, and allowed to air dry. Large colorless plates of **1** were collected. Yield: 94% (based on Bi). Elemental Analysis: Calc. (Obs.): C, 30.27 (30.26); H, 2.25 (2.18); N, 2.08, (2.13 %). Raman **1** ῡ = 1528, 1479, 1400,1315, 1202, 1124, 1009, 835, 392 cm^{-1}.

$[Hpy]_3[Bi_2(TDC)_4(HTDC)H_2O)] \cdot 0.74H_2O$ (2) and **$(Hpy)_2[Bi(TDC)_2(HTDC)] \cdot 0.36H_2O$ (3)**

Bismuth nitrate (0.0182 grams, 0.04 mmol), H_2TDC (0.054 grams, 0.3 mmol), water (2 mL), and ethanol (1 mL) were loaded into a 10 mL glass vial. Pyridine (40 μL, 0.5 mmol) was used to adjust the final pH_i between 4-5. The glass vial was capped and placed on the benchtop at room temperature. After five days, the products were filtered, washed in water and ethanol, and allowed to dry ($pH_f \approx$ 4-5). A white, microcrystalline phase identified via powder X-ray

diffraction as **2** along with colorless plates of compound **3** were collected. Colorless plates of compound **2** suitable for structural analysis by single crystal X-ray diffraction could be prepared by heating compound **1** at 50 °C overnight; however, a complete phase conversion was not observed. Raman **2** $\tilde{\upsilon}$ = 1648, 1576, 1472, 1394, 1315, 1114, 1006, 831, 462, 389 cm^{-1}. Raman **3** $\tilde{\upsilon}$ = 1650, 1590, 1463, 1397, 1318, 1111, 1006, 831 cm^{-1}.

Lanthanide-Doped Analogs of 1 and 3

In order to dope **1** and **3**, an aliquot of the respective lanthanide nitrate hydrate solution *vide infra* was added prior to crystallization of the bismuth-only phases with a Bi:Ln molar ratio of approximately 9:1. To obtain the doped analog of **1**, the lanthanide solution was added two days after the start of the reaction, while a white suspension was still present. In the case of **3**, the lanthanide solution was added prior to visual evidence of crystallization of **3**. When the lanthanide solution was added at the beginning of the reaction, phase separation (identified based on differences in the morphologies of the Bi- and Ln-TDC phases) was observed, with the respective Ln-TDC phase crystallizing prior to the Bi-TDC phase.

$Hpy[Bi_{1-x}Ln_x(TDC)_2(H_2O)]\cdot 1.5H_2O$ ($Bi_{1-x}Ln_x$-1)

The syntheses follow that of compound **1**. After 2 days, an aliquot of an aqueous 0.025M lanthanide nitrate solution (167 μL, 0.00417 mmol) was added to the glass vial which contained a white suspension. After five to seven additional days, the solution was clear and colorless, and colorless crystals had deposited at the bottom of the vial. The products were filtered, washed in water and ethanol, and allowed to air dry. Clear, colorless plates of **$Bi_{1-x}Ln_x$-1** were observed. Yield: 80-90% (based on Bi). Elemental Analysis: Ln=Nd, Calc. (Obs.): C, 30.39 (30.43); H, 2.25 (2.29); N, 2.06 (2.15%); Ln=Sm, Calc. (Obs.): C, 30.44 (30.31); H, 2.25 (2.23), N, 2.09, (2.14%); Ln=Eu, Calc. (Obs.): C, 30.29 (30.58); H, 2.24 (2.11); N, 2.08, (2.28%); Ln=Tb, Calc. (Obs.): C, 30.29 (30.63); H, 2.24 (1.76); N, 2.08, (2.05 %); Ln= Dy, Calc. (Obs.): C, 30.32 (30.44); H, 2.24 (2.06); N, 2.08, (2.17%); Ln= Yb, Calc. (Obs.): C, 30.31 (30.22); H, 2.24 (2.10); N, 2.08, (2.20%).

$[Bi_{0.99}Eu_{0.01}(TDC)_2(HTDC)(Hpy)_2]$($Bi_{0.99}Eu_{0.01}$-3)

The syntheses follow that of **2** and **3**. Two days after capping the glass vial, an aliquot of a 0.025M europium nitrate solution (167 μL, 0.00417 mmol) was added to the reaction. After two more days, the products were filtered, washed in water and ethanol, and allowed to dry under ambient conditions. Single crystals of the europium compound **$Bi_{0.99}Eu_{0.01}$-3** and a nonluminescent, white, microcrystalline minor phase identified as undoped **2** (via PXRD) were present. **$Bi_{0.99}Eu_{0.01}$-3** could be identified by visual inspection under a UV lamp and was manually separated from **2**. Yield: 89% (based on Bi). Elemental Analysis: Ln=Eu, Calc. (Obs.): C, 38.00 (37.54); H, 2.14 (2.02); N, 3.17, (3.12). Note that because **$Bi_{0.99}Eu_{0.01}$-3** was manually separated from **2** under a UV lamp, using the luminescence of Eu as a guide, we did not prepare the other Ln doped analogs.

[Eu(TDC)(NO_3)(H_2O)] (4)

An aliquot of a 0.0267 M solution of europium nitrate in glacial acetic acid (1.5 mL, 0.04 mmol), an aliquot of a 0.2 M solution of H_2TDC in ethanol (1.5 mL, 0.3 mmol), and pyridine (40 μL, 0.5 mmol) were loaded into a 10 mL glass vial. The vial was capped and left on the benchtop at room temperature. Colorless crystals formed overnight and deposited at the bottom of the vial. The products were filtered, washed in water and ethanol, and allowed to air dry. Large colorless plates identified as **4** were collected. Though not readily apparent in the powder pattern, a minor phase impurity identified via elemental analysis precluded subsequent characterization that required bulk purity (Fig. S9). Raman $\tilde{\upsilon}$ = 1546, 1476, 1405, 1325, 1217, 1131, 1033, 793, 760, 680 cm^{-1}.

[Eu_2(TDC)$_3$(H_2O)$_9$]·5H_2O (5)

Europium nitrate (0.0178 grams, 0.04 mmol), H_2TDC (0.054 grams, 0.3 mmol), water (2 mL), and ethanol (1 mL) were loaded into a 10 mL glass vial. Pyridine (40 μL, 0.5 mmol) was used to adjust the final pH between 3-4. The glass vial was capped and placed on the benchtop at ambient temperature. After one day, the products were filtered, washed with water and ethanol, and allowed to dry under ambient conditions. Colorless needles of **5** were collected. Yield= 39.5% (based on Eu). Elemental Analysis: Calc. (Obs.): C, 20.27 (20.63); H, 3.21 (3.07). Raman $\tilde{\upsilon}$ = 1539, 1521, 1479, 1409, 1317, 1120, 1034, 822, 758 cm^{-1}.

Single crystal X-ray diffraction

Single crystals of **1-5** were selected from the bulk and mounted on MiTeGen micromounts in paratone. Single crystal X-ray diffraction data were collected at 100(2) K on a Bruker D8 Quest diffractometer equipped with an I*u*S X-ray source (Mo-Kα radiation; λ=0.71073 Å) and a Photon 100 CMOS detector. Data were integrated using the SAINT software package included with APEX2.[63, 64] An absorption correction was applied using a multi-scan technique in SADABS.[65] The structures were solved using direct methods via SHELXT and refined by full-matrix least-squares on F2 using the SHELXL software in WinGX.[66, 67] Crystallographic data for compounds **1- 5** are provided in Table 1, and the resulting CIF data are available in the ESI. The structure of **4** was previously reported;[46] however, the data were previously collected at 293 K, and thus, for the sake of comparison with the structures reported in this work, a low temperature dataset for **4** was collected at 100 K. Due to crystallographic challenges involving disordering of the pyridinium rings as well as residual electron density near the metal centers, only a preliminary structure refinement of **2** is reported. Further details of the disorder and crystallographic refinement are provided in the ESI. Crystallographic data were deposited in the Cambridge Structural Date Centre (CCDC), and may be found at http://www.ccdc.cam.ac.uk/ by using reference numbers 1589868, 1589869, 1589870, 1589871, and 1589872.

Table 1 Crystallographic Structure Refinement Details for compounds **1- 5**.

	1	**2**	**3**	**4**	**5**
Formula	$C_{17}H_{15}BiNO_{10.50}S_2$	$C_{45}H_{29}Bi_2N_3O_{22.90}S_5$	$C_{28}H_{19.72}BiN_2O_{12.36}S_3$	$C_6H_4EuNO_8S$	$C_{18}H_{34}Eu_2O_{26}S_3$
MW ($gmol^{-1}$)	674.40	1541.35	887.11	402.12	1066.57
T (K)	100(2)	100(2)	100(2)	100(2)	100(2)
λ (K α)	0.71073	0.71073	0.71073	0.71073	0.71073
μ (mm^{-1})	8.869	7.479	6.484	6.081	3.992
Crystal System	Monoclinic	Triclinic	Monoclinic	Monoclinic	Orthorhombic
Space Group	$P2_1/n$	P-1	$P2_1/n$	$P2_1/c$	Pbcn
a (Å)	8.5780(6)	8.8032(6)	8.913(3)	9.9248(4)	36.9994(14)
b (Å)	25.4265(16)	9.9506(7)	35.065(13)	14.3297(6)	7.5906(3)
c (Å)	10.0899(6)	30.2245(19)	9.735(3)	7.7249(3)	23.8697(9)
α (°)	90	88.023(2)	90	90	90
β (°)	111.421(2)	87.299(2)	110.591(13)	102.940(1)	90
γ (°)	90	68.843(2)	90	90	90
Volume ($Å^3$)	2048.7(2)	2465.9(3)	2847.9(17)	1070.73(7)	6703.7(4)
Z	4	2	4	4	8
R_{int}	0.0341	0.0617	0.0493	NA[a]	0.0977
R ($I > 2\sigma$)	0.0230	0.0490	0.0504	0.0319	0.0392
wR_2	0.0392	0.0949	0.1072	0.0724	0.0783
GooF	1.1486	1.090	1.112	1.077	1.046
Residual density (max/min)	0.772/ -1.318	3.86/-3.03	2.075/ -2.703	0.989/-1.197	0.859/ -0.923
CCDC No.	1589868	1589869	1589870	1589871	1589872

[a] The refinement of **4** was processed as a two component twin and therefore a R_{int} is not reported.

Characterization methods

Powder patterns were collected for the bulk samples from which **1-5** were isolated using Cu-Kα radiation (λ = 1.542 Å) on a Rigaku Ultima IV X-ray diffractometer from 3-40° in 2θ with a step speed of 1 degree/min. Raman spectra were collected for single crystals pulled from the bulk using an excitation source of 532 nm (maximum power=100mW) on a Horiba LabRAM HR Evolution Raman Spectrometer. Spectra were recorded from 200 to 2000 cm^{-1} using 20

accumulations and a laser power of 3.2 to 10%. For **4** and **5**, an excitation source of 405 nm was used to avoid interference from europium luminescence. The laser power was set to 50%. Infrared spectra were collected either on powdered samples prepared as KBr pellets on a Perkin Elmer Spectrum Two FTIR Spectrometer or as powdered samples directly measured on a Perkin Elmer Frontier Spectrometer with a UATR attachment of diamond/ZnSe. Combustion elemental analysis was carried out using a Perkin Elmer Model 2400 Elemental Analyzer on the bulk phases. Thermogravimetric analyses were conducted on a TA Instruments Q50 Thermogravimetric Analyzer under flowing N_2 (flow rate=10 mL/min).

Inductively Coupled Plasma-Mass Spectrometry

Inductively coupled plasma-mass spectrometry was carried out on an Agilent 7700 ICP-MS to determine the bismuth:lanthanide ratio for the doped phases, $\mathbf{Bi_{1-x}Ln_x}$**-1** (where Ln=Nd, Sm, Eu, Tb, Dy, and Yb) and $\mathbf{Bi_{0.99}Eu_{0.01}}$**-3**. Between 15 to 30 mg of each sample was dissolved in 5% HNO_3 under slight heating and stirring. A calibration curve was made for each element (Bi, Nd, Sm, Eu, Tb, Dy, and Yb) using eight concentrations (10 ppb, 50 ppb, 100 ppb, 500 ppb, 1000 ppb, 1500 ppb, 2000 ppb, and 3000 ppb). All solutions were made using 5% HNO_3. The ratio of bismuth:lanthanide was then calculated from the respective calibration curve.

Photoluminescence measurements

Solid state luminescence spectra were collected on a Horiba PTI QM-400 system. Excitation and emission spectra as well as lifetime measurements were collected for powdered samples and/or crystals isolated from the bulk sample. The samples were placed between two glass slides and collected using fluorimeter slit widths of 1-3 nm for the visible emitters and 6 nm for the NIR emitters. The 1st and 2nd harmonic oscillations from the excitation source were blocked using longpass filters (400 nm or 420 nm). In all cases, the wavelength of the peak of maximum intensity in the excitation spectrum was used to generate the emission spectrum. Lifetime and quantum yield measurements were run in triplicate and the reported values are the average of these runs. Lifetime measurements were carried out with a lamp frequency of 300 Hz using 10,000 shots, and the exponential decay curves were fit using OriginPro 8.5. Quantum yield values were collected on an undiluted crystalline sample in a Teflon powder holder using an 8.9 cm integrating sphere coated in Spectralon fluoropolymer with 1 nm slit widths. The spectra recorded were background corrected using a blank sample holder and corrected for the wavelength dependence of the spectrofluorometer, sampling optics, and integrating sphere. The quantum yields (φ_{tot}) were determined according to the following equation (Eq. 1):

$$\varphi_{tot} = \left(\frac{E_s - E_b}{L_b - L_s}\right) \quad (1)$$

where E_s is the integrated emission spectrum of the crystalline sample, E_b is the integrated emission spectrum of a blank (empty Teflon sample holder), L_s is the sample absorption at the excitation wavelength, and L_b is the blank absorption at the same excitation wavelength.

The radiative lifetime (τ_r), and subsequently, the overall sensitization efficiency (n_{sens}) and intrinsic quantum yield (φ_{Eu}) for the europium phases were determined using Eqs. 2-4:[9]

$$\frac{1}{\tau_r} = A_{MD} n^3 \left(\frac{I_{tot}}{I_{MD}}\right) \quad (2)$$

where A_{MD} is the spontaneous emission probability of the $^5D_0 \rightarrow {}^7F_1$ transition (14.65 s^{-1}), n is the refractive index for solid samples (1.5), and I_{tot}/I_{MD} is the ratio of the total integrated emission ($^5D_0 \rightarrow {}^7F_J$, J=0-6) to the integrated intensity of the magnetic dipole transition ($^5D_0 \rightarrow {}^7F_1$),

$$\varphi_{Eu} = \frac{\tau_{obs}}{\tau_r} \quad (3)$$

where τ_{obs} is the observed lifetime calculated from the exponential decay curve,

$$\eta_{sens} = \frac{\varphi_{tot}}{\varphi_{Eu}} \quad (4)$$

In addition to the luminescent measurements described above, to support homogeneity of doping, spectra were also collected at multiple points and focusing depths along the length of a single crystal of **$Bi_{0.99}Eu_{0.01}$-1** using a Horiba LabRAM HR Evolution Raman Spectrometer with an excitation source of 405 nm (Fig. S38). Spectra were collected over 570 to 650 nm. All luminescence measurements were performed at room temperature in air.

Results

Syntheses

The synthesis of three bismuth(III) thiophenecarboxylates from aqueous conditions was explored. The bismuth precursor as well as the solvent system were found to have some impact on phase formation. Compounds **2** and **3** were isolated from the reaction of bismuth nitrate, H_2TDC, and pyridine with a molar ratio of 1:7.5:12.5, respectively. Use of bismuth oxide similarly yielded compounds **2** and **3**; however, bismuth chloride resulted in the formation of **1** along with **2** as a minor phase. Various solvents (i.e. water, ethanol, acetic acid) were explored in an effort to arrive at phase pure products. A combination of acetic acid and ethanol allowed for isolation of **1** as a pure phase, as confirmed by PXRD and elemental analysis. Attempts to isolate **3** as a phase pure product; however, by varying solvent (i.e. water, water/ethanol, ethanol) were unsuccessful, but did allow for optimization of the estimated yield. Interestingly, despite having been synthesized at similar initial pH, compounds **2** and **3** consist of protonated HTDC whereas **1** is built from fully deprotonated TDC. As the pK_{a1} and pK_{a2} of H_2TDC in 30% EtOH/H_2O are 3.2 and 4.3, respectively, [68] protonation of TDC is likely given the pH of the reaction solutions. Attempts to realize a hydrothermal or solvothermal product proved unsuccessful, resulting in the recrystallization of starting material.

Structure descriptions

Hpy[Bi(TDC)$_2$(H$_2$O)]·1.5H$_2$O (1)

The asymmetric unit of **1** is built from one crystallographically unique Bi^{3+} metal center, two unique κ^2-TDC ligands, one coordinated water molecule, and one pyridinium cation. Each Bi^{3+} metal center is nine-coordinate, bound to eight O atoms from four κ^2-TDC ligands and one O atom from a bound water molecule (Fig. 1). The Bi-O bond distances vary from 2.351(2) to 2.685(2) Å, with noticeable asymmetry of the Bi-O bond lengths, (e.g. Bi1-O11 and Bi1-O12 (2.629(2) and 2.351(2) Å, respectively, and Bi1-O21 and Bi1-O22 2.389(2) and 2.562(2) Å, respectively). The Bi-O bond lengths of the positionally disordered water are 2.530(4) and 2.522(5) Å for Bi1-O30 and Bi1-O30B, respectively. Two of the TDC ligands bridge the bismuth metal center along the [-110] to form zigzag chains as shown in Fig. 2a, with Bi···Bi distances of 10.814(4) Å. These chains are then connected down the [101], with a Bi···Bi distance of 10.591(6) Å, by the remaining TDC ligands resulting in 2D anionic sheets that are charge balanced by pyridinium cations (Fig. 2b). As shown in Fig. 2c and 2d, an additional sheet is generated through symmetry, resulting in an interpenetrated network. The sheets stack down the [010], where the bound water molecule, O30, points into the interlayer as seen in Fig. 3. Intermolecular π-π stacking and hydrogen-bonding interactions help stabilize the structure. There are two non-variable solvent water molecules (O40 and O41) present in the lattice, with O41 being only partially occupied (49.6%). The solvent water molecules display moderate hydrogen bonding interactions to the oxygen atom of the bound water, with O(40)-H···O30=2.775(5) Å, O(40)-H···O30B=2.768(5) Å, O(41)-H···O30= 2.673(7) Å, and O(41)-H···O30B= 2.499(7) Å. The proton of the pyridinium nitrogen shows acceptable hydrogen bonding interactions with the fully occupied solvent water, with N(50)-H···O40= 2.728(4) Å. Furthermore, H-bonding interactions between solvent water molecules and a bound carboxylate group, O(41)-H···O23= 2.606(7) Å and O(40)-H···O24= 2.626(4) Å, are present in the structure. The compound is then further stabilized by strong π-π interactions occurring between adjacent thiophene rings across the interlayer as shown in Fig. 3. The π-π interactions were determined through Platon[70] with the distance between the centroids C_{TDC}···C_{TDC}=3.5311(2) Å and a slip angle of 20.9°.

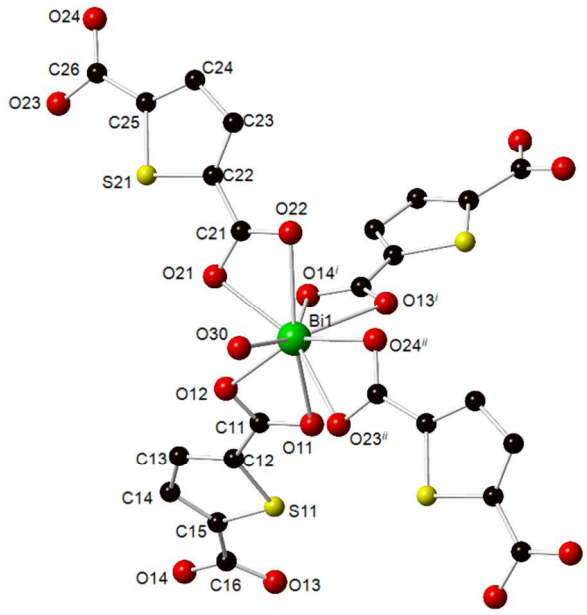

Fig. 1 Illustration of the local coordination sphere of Bi1 in **1**. Hydrogen atoms, pyridinium, and solvent water molecules have been omitted for clarity. Bi=green, S=yellow, O=red, C=black. Symmetry operators: (i) x - 1/2, -y + 3/2, z + 1/2; (ii) x - 1, y, z - 1.

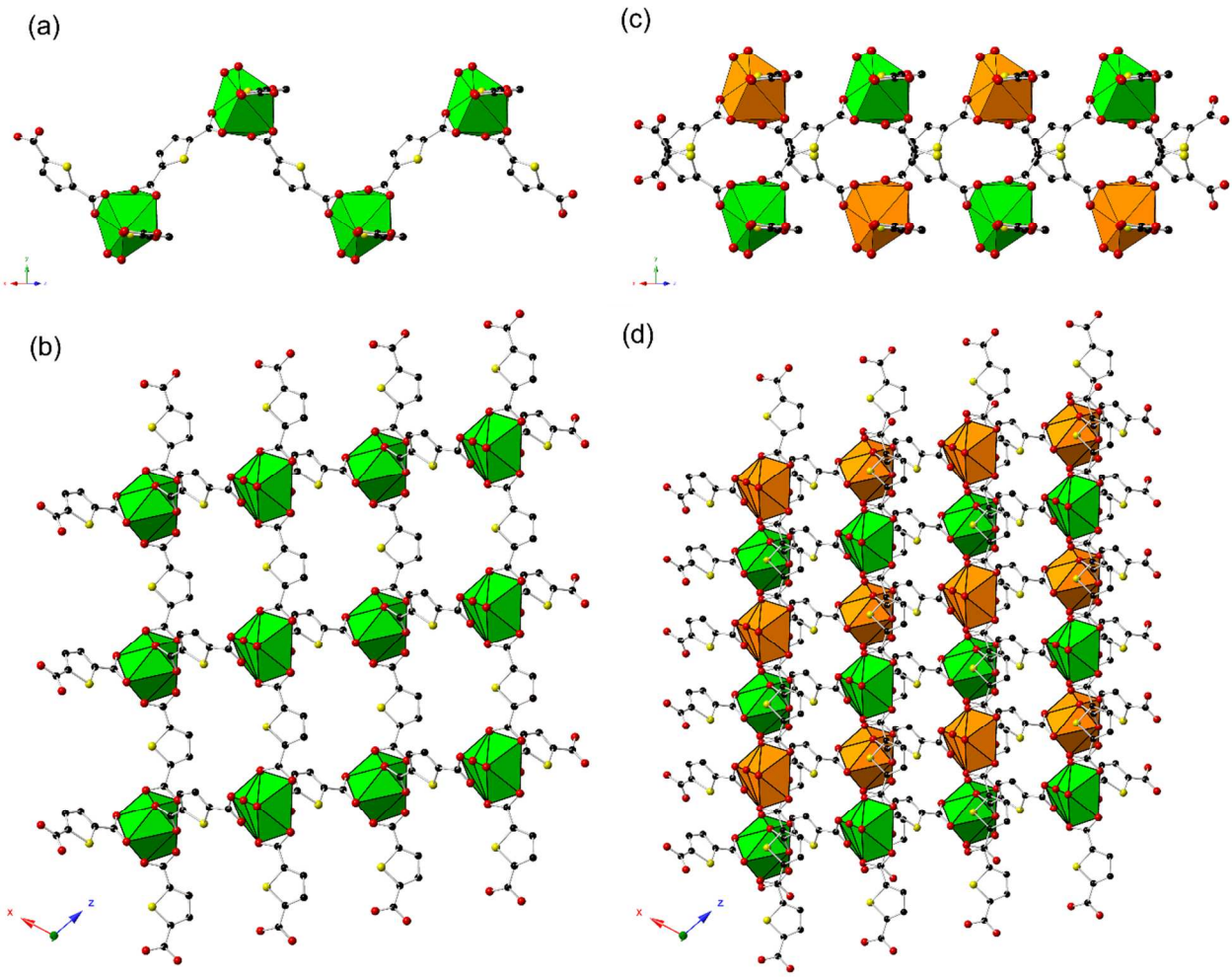

Fig. 2 Polyhedral representation of **1** highlighting the connectivity of (a) one single chain, (b) one sheet, (c) interpenetrated chains, and (d) interpenetrated sheets. Both (a) and (c) are viewed down the [101], while (b) and (d) are shown down the [010]. Hydrogen atoms, solvent water molecules, and pyridinium cations have been omitted for clarity. Bi=green or orange polyhedra, O=red, S=yellow, C=black.

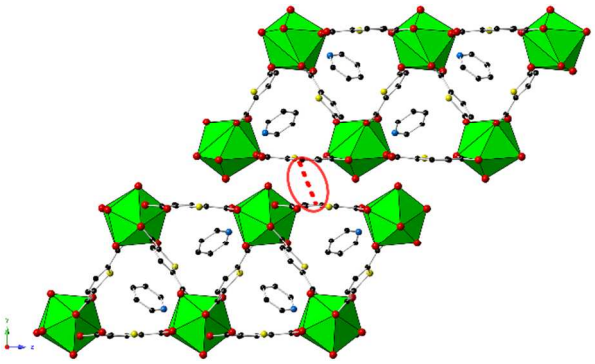

Fig. 3 Packing diagram of **1** viewed along [100]. For simplicity, only one sheet is depicted. Hydrogen atoms and solvent water molecules have been omitted for clarity. Red dashed line and circle highlight π-π interactions. Bi=green polyhedra, O=red, S=yellow, N =blue, C=black.

$[Hpy]_3[Bi_2(TDC)_4(HTDC)H_2O)]\cdot xH_2O$ (2)

The asymmetric unit of **2** consists of two crystallographically unique Bi^{III} metal centers (Bi1 and Bi2), four unique κ^2-TDC ligands, one unique κ^1-HTDC ligand, and one coordinated water molecule. Additionally, there are three disordered pyridinium rings per formula unit that charge balance the bismuth anionic unit. Bi1 is ten-coordinate, bound to ten O atoms from five κ^2-TDC ligands, and Bi2 is nine-coordinate, bound to nine O atoms from three κ^2-TDC, one κ^2-HTDC ligand, and one water molecule (Fig. 4). The Bi1-O bond lengths range from 2.3546(2) to 2.6578(2) Å, while Bi2-O range from 2.3625(2) to 2.7981(2) Å, again displaying asymmetry in the Bi-O bond lengths as observed in **1**. The Bi2-O(91)H_2 distance is 2.564(9) Å. Bi1 and Bi2 are bridged through one of the TDC ligands, with a Bi···Bi distance of 10.771(11) Å, propagating into zigzag chains along [110] similar to the connectivity in **1** (Fig. 5). The remaining TDC further link the resulting chains down the [1-10] into sheets. Additional chains are then generated by symmetry, forming a 2D interpenetrated network like that in **1**. The sheets pack along the [001], with alternating HTDC and bound water molecules pointing into the interlayer spacing (Fig. 6). The closest Bi1···Bi1 distance between sheets is 10.096(5) Å and 6.197(5) Å for Bi2···Bi2, demonstrating the effect of the alternating ligation on the packing of the sheets. Furthermore, π-π interactions from TDC ligands across the interlayer formed by Bi2 metal centers are observed with centroid-centroid distances given as $C_{TDC}\cdots C_{TDC}$=3.5487(2) Å with a slip angle of 20.2°. Crystallographic challenges precluded satisfactory refinement of the solvent water molecules, and therefore, these interactions are not commented on herein.

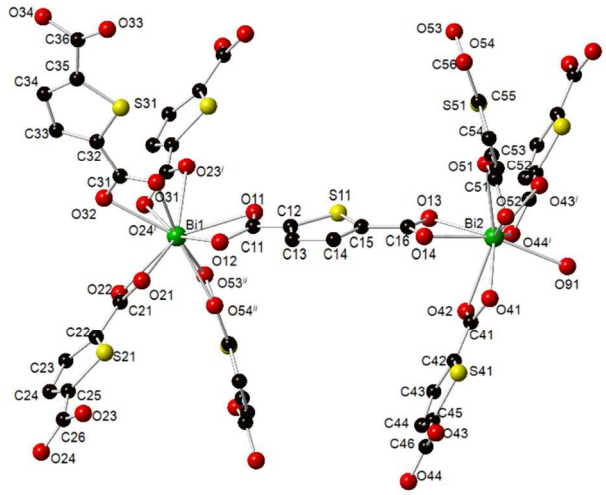

Fig. 4 Illustration of the local coordination spheres of Bi1 and Bi2 in **2**. Hydrogen atoms, pyridinium cations, and solvent water molecules have been omitted for clarity. Bi=green, S=yellow, O=red, C=black. Symmetry operators: (i) x - 1, y + 1, z; (ii) x - 1, y - 1, z.

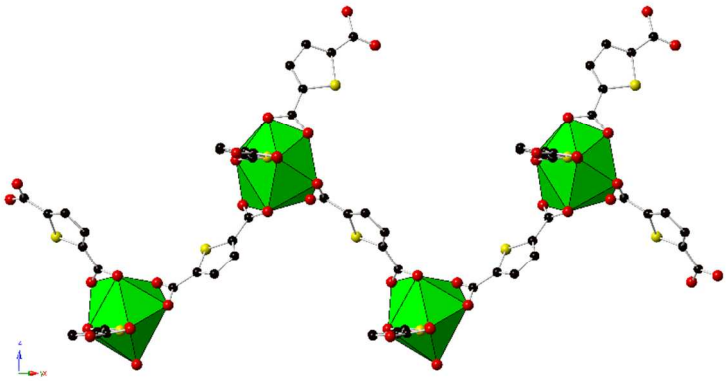

Fig. 5 Polyhedral representation of **2** viewed down the [-110] of one chain. Hydrogen atoms as well as solvent water molecules and pyridinium cations have been omitted for clarity. Bi=green polyhedra, O=red, S=yellow, C=black.

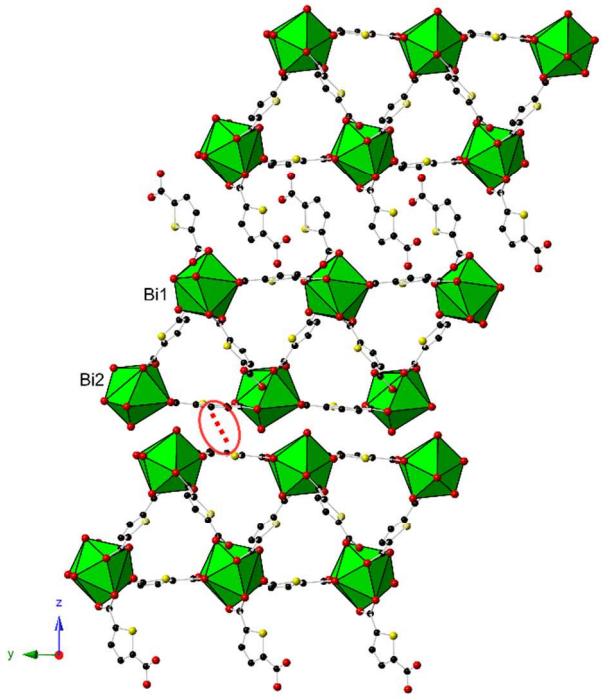

Fig. 6 Packing diagram of **2** viewed in the [100]. For simplicity, only one sheet is depicted. Red dashed line and circle highlight π-π interaction. Hydrogen atoms as well as solvent water molecules and pyridinium have been omitted for clarity. Bi=green polyhedra, O=red, S=yellow, C=black.

$(Hpy)_2[Bi(TDC)_2(HTDC)]\cdot 0.36H_2O$ (3)

The asymmetric unit of compound **3** consists of one crystallographically unique Bi^{III} metal center, two κ^2-TDC, one κ^1-HTDC, two pyridinium cations, and one partially occupied water. Each Bi^{III} metal center is ten-coordinate, bound to ten O atoms from four κ^2-TDC ligands and one κ^2-HTDC ligand as shown in Fig. 7. The Bi-O bond lengths range from 2.360(4) to 2.737(4) Å, displaying noticeable and more pronounced asymmetry in the Bi-O(carboxylate) bond distances than those of **1** and **2**, e.g. Bi1-O11=2.694(5) Å and Bi1-O12=2.402(5) Å. One long Bi1···O34 interaction is seen with a distance of 3.0359(3) Å. The bismuth metal center is bridged through a TDC ligand along the [-101] to another bismuth center (Bi···Bi=10.827(3) Å), forming zigzag chains akin to those observed in **1** and **2** (Fig. 8). These units are further connected through another TDC ligand, linking bismuth metal centers in the [101] direction (Bi···Bi=10.639(10) Å) to form thick 2D sheets. These sheets stack down the [010], with the shortest Bi···Bi distance found to be 10.128(4) Å across adjacent sheets. Terminal HTDC ligands point into the interlayer space between the sheets. Hydrogen-bonding is observed between the protonated OH of the terminal HTDC ligand and the partially occupied water, with O(14)H···O(61) donor-acceptor distances of 2.744(10) Å, and π-π stacking interactions are observed between the thiophene ring of the terminal HTDC and a nearby pyridinium cation, with centroid-centroid distances of $C_{HTDC}\cdots C_{Hpy}$=3.7147(14) Å with a slip angle of 24.1° (Fig. 9).

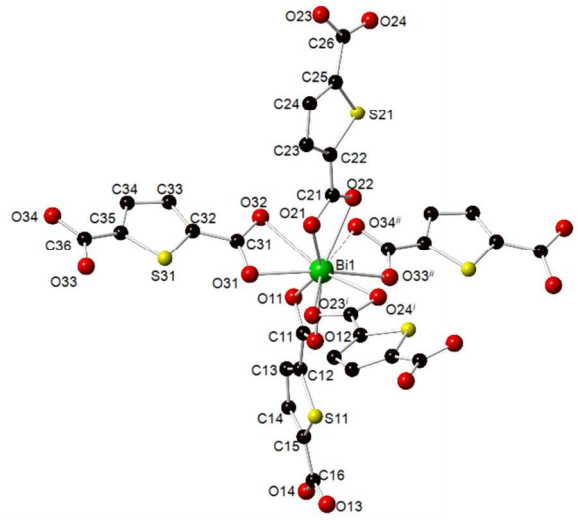

Fig. 7 Illustration showing the local coordination sphere of Bi1 in **3**. Hydrogen atoms, pyridinium, and solvent water molecules have been omitted for clarity. Bi=green, S=yellow, O=red, C=black. Symmetry operators: (i) x - 1/2, -y + 3/2, z + 1/2; (ii) x + 1, y, z + 1.

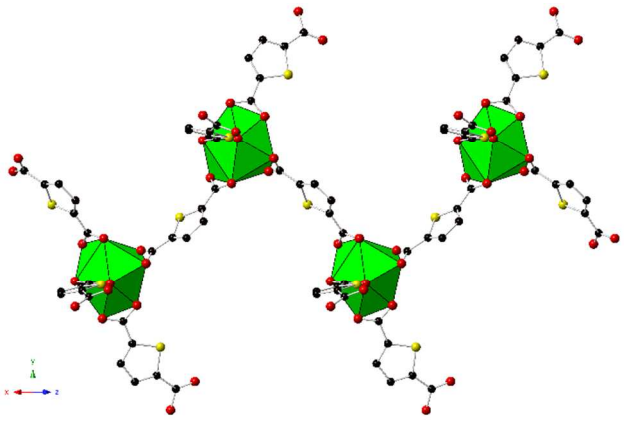

Fig. 8 Polyhedral representation of **3** down the [101]. Hydrogen atoms as well as solvent water molecules and pyridinium cations have been omitted for clarity. Bi=green polyhedra, O=red, S=yellow, C=black.

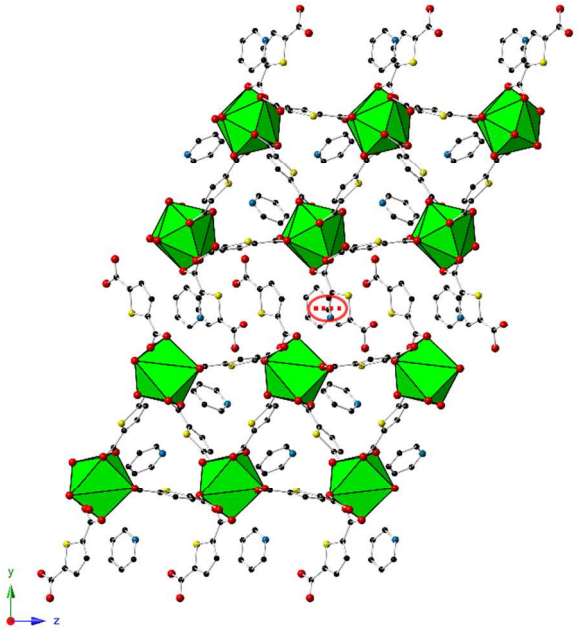

Fig. 9 Packing diagram of **3** viewed down the [100]. Red dashed line and circle highlight the π-π interaction between the HTDC and nearby pyridinium cation. For simplicity, only two sheets are shown. Hydrogen atoms and solvent water molecules as well as disorder in the pyridinium rings have been omitted for clarity. Bi=green polyhedra, O=red, S=yellow, N=blue, C=black.

[Eu(TDC)(NO_3)(H_2O)] (4)

Compound **4** has been previously reported,[35] and as such, only a brief structural description is provided. The asymmetric unit of **4** consists of one unique Eu^{III} metal center, one κ^1-TDC ligand, one nitrate ion, and one water molecule. Each Eu^{III} metal center is eight-coordinate and bound to three O atoms from three κ^1-TDC ligands, three O atoms from one κ^1-nitrate and one κ^2-nitrate, and one O atom from a bound water molecule, forming a dodecahedron coordination geometry. The Eu1-O bond distances of the carboxylates vary from 2.336(3) to 2.366(4) Å. Eu-O distances of the bound water molecule and the nitrate are 2.417(4) Å and 2.389(3) to 2.525(3) Å, respectively. The metal centers are bridged through the TDC ligands as well as the bound nitrates to form a 3D network.

[Eu_2(TDC)$_3$(H_2O)$_9$]·5H_2O (5)

Compound **5** crystallizes in the orthorhombic space group, *Pbcn*, and consists of three crystallographically unique TDC ligands and nine coordinated water molecules. Eu1 is eight coordinate, forming a square antiprism coordination geometry, and is bound to three O atoms from three κ^1-TDC ligands, two O atoms from one κ^2-TDC ligand, and three water molecules (Fig. 10). Eu2 also adopts a square antiprism coordination geometry bound to two O atoms from two κ^1-TDC ligands and six coordinated water molecules (Fig. 10). The Eu1-O bond distances of the carboxylates and water molecules vary from 2.288(4) to 2.486(4) Å and 2.361(4) to 2.487(5) Å, respectively. The Eu2-O bond distances of the carboxylate O atoms are 2.369(4) Å

(Eu2-O24) and 2.375(4) Å (Eu2-O32). The Eu2-O distances for the bound water molecules range from 2.382(5) to 2.472(5) Å. Eu1 is bridged to one Eu2 metal center through the carboxylate of a TDC ligand in the [001] direction as well as a second Eu2 metal center through the TDC ligand in the [100] direction as shown in Fig. 11. Further, Eu1 is bound to a symmetry equivalent Eu1 through two TDC ligands along the [100]. These europium units extend to form staircase-like 2D sheets along the [100] and [001] (Fig. 12a). Additionally, a second chain is generated through symmetry resulting in an interpenetrated network, as illustrated by the purple and blue polyhedra in Fig. 11b. The sheets are further stabilized by both hydrogen-bonding interactions and π-π stacking. The five solvent water molecules display moderate hydrogen bonding interactions to the oxygen atom of the bound water, namely O(61)-H···O41=2.788(6) Å, O(62)-H···O52=2.809(7) Å, O(63)-H···O52=2.663(7) Å, O(64)-H···O53=2.811(7) Å, and O(65)-H···O53=2.758(7) Å. Moderate π-π interactions occur between thiophene rings of the TDC ligands that bridge Eu1 to a symmetry equivalent Eu1 in the same sheet, and between two thiophene rings in adjacent interpenetrated sheets (Fig. 12a and 12b, respectively). The π-π interactions were calculated from Platon, and given as the distances between the centroids $C_{TDC}\cdots C_{TDC}$=3.5832(1)Å with a slip angle of 18.2° and $C_{TDC}\cdots C_{TDC}$=3.7999(2) Å and a slip angle of 14.1°, respectively.

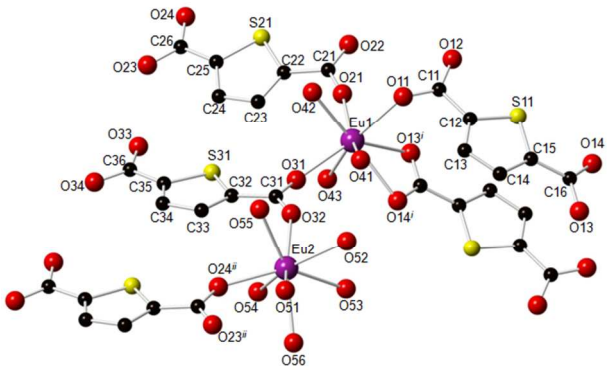

Fig. 10 Illustration showing the connectivity of Eu1 and Eu2 in **5**. Bound water molecules are labeled as O41-O43 and O51-O56. Hydrogen atoms and solvent water molecules have been omitted for clarity. Eu=purple, S=yellow, O=red, C=black. Symmetry codes: (i) -x + 1, -y, -z + 1; (ii) -x + 1/2, -y + 1/2, z + 1/2.

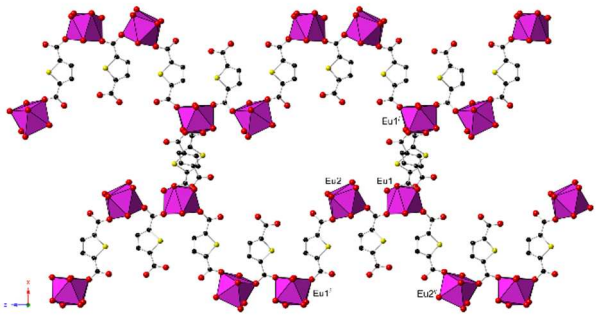

Fig. 11 Polyhedral representation of **5** displaying one sheet viewed down the [010]. Hydrogen atoms and solvent water molecules have been omitted for clarity. Eu=purple polyhedra, O=red, S=yellow, C=black. Symmetry codes: (i) -x + 1, -y, -z + 1; (ii) -x + 1/2, -y + 1/2, z + 1/2.

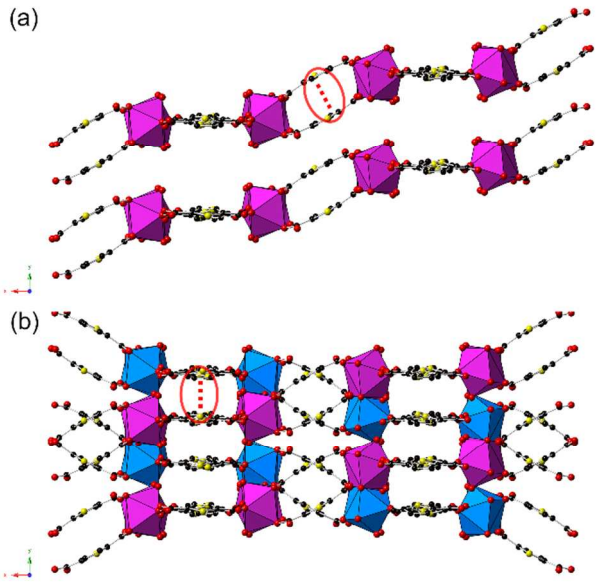

Fig. 12 Packing diagram of **5** shown along [001] illustrating (a) two parallel sheets and (b) four interpenetrated sheets. Connectivity of the Eu^{3+} metal centers is shown by either the purple or blue polyhedra. Red dashed lines highlight π-π stacking interactions. Hydrogen atoms as well as solvent water molecules have been omitted for clarity. Eu=purple or blue polyhedra, O=red, S=yellow, C=black.

Raman spectroscopy

Raman spectra were collected for a powdered sample of 2,5-thiophenedicarboxylic acid as well as single crystals of **1- 5** (Fig. S11-S16). The spectrum for each of the bismuth compounds show characteristic ligand and pyridinium bands, whereas for **5**, characteristic ligand peaks are observed. In compounds **2** and **3**, the peak attributed to the stretching of the carbonyl group of H_2TDC, which typically observed around 1660 cm^{-1} is present; however, it is slightly shifted to 1648 and 1650 cm^{-1}, respectively.[59] In compounds **1**, **4**, and **5**, this peak is noticeably absent,

which is consistent with full deprotonation of the TDC ligands as supported by the crystal structure. Very strong peaks are seen between 1460 and 1480 cm^{-1} in the spectra of **1-5** as well as that collected for the ligand, which may be attributed to C=C stretches from the thiophene rings. Multiple peaks are also observed between 1000 and 1400 cm^{-1}, which can be attributed to overlapping bands from COO^-, C-H, and ring vibrations from both the thiophene and/or pyridinium rings.

Thermal behavior

The thermal stabilities of compounds **1**, **$Bi_{0.99}Eu_{0.01}$-3,** and **5** were investigated over 25 °C to 600 °C under flowing N_2 (Fig. S17-S19). For **1**, the total weight loss was 60.26%, beginning around 50 °C with full decomposition seen by 330 °C. The thermogravimetric curve for compound **$Bi_{0.99}Eu_{0.01}$-3** exhibited a total weight loss of 51.86% beginning at 30 °C and ending at 325 °C. Powder X-ray diffraction data were collected for each of the products obtained after thermal decomposition; however, full assignment of the resulting phase(s) was unsuccessful. The decomposition products of **1** and **$Bi_{0.99}Eu_{0.01}$-3** have similar spectra, indicating related end products (Fig. S23). Furthermore, the IR spectra of the thermally decomposed products show peaks at 496, 600, 967, 1038, 1098, and 1155 cm^{-1} for **1** and a peak at 1095 cm^{-1} for **$Bi_{0.99}Eu_{0.01}$-3**, consistent with the presence of a sulfate phase (Fig. S20-S21).[71] This is also consistent with reported decomposition products of other metal thiophenecarboxylate compounds.[45, 72, 73] The peaks around 1384 cm^{-1} could be attributed to a carbonate species formed upon exposure to air after thermal decomposition.[71] A broad peak at 3433 and 3454 cm^{-1} seen for **1** and **$Bi_{0.99}Eu_{0.01}$-3**, respectively, is possibly a hydrated phase forming after decomposition. For **5**, thermal decomposition began immediately, with a 66.51% total weight loss beginning at 25 °C and concluding around 495 °C. An IR spectrum of the thermal decomposition product revealed major peaks at 598 and 1060 cm^{-1}, again consistent with decomposition to some sulfate species as observed in **1** and **$Bi_{0.99}Eu_{0.01}$-3** (Fig. S22). The broad peak at ca. 3350 cm^{-1} could be formation of a hydrated phase after decomposition.

Doping

Efforts to dope frameworks often result in one of three outcomes: a) site substitution or statistic replacement of the metals, b) formation of a new bimetallic phase, or c) phase separation.[26] In the case of **$Bi_{1-x}Ln_x$-1** and **$Bi_{0.99}Eu_{0.01}$-3**, incorporation of the Ln ion into the Bi framework is seen, as confirmed by powder XRD, ICP-MS, Raman, and luminescence data. Upon addition of the lanthanide solution at the start of the reaction, separation of the Ln- and Bi-TDC phases was observed. Adding the lanthanide solution subsequent to complete crystallization of the Bi-TDC phase resulted in no incorporation of the lanthanide ion into the structure. These results may be attributed to differences in the solubility and/or crystallization kinetics of the Bi- and Ln- phases which we hypothesize may be overcome, albeit to a very limited extent given the doping levels, by first allowing the Bi-ligand units to form in solution prior to addition of the Ln metal center. The ratio of europium doped into each Bi-TDC compound was determined via ICP-MS for

Ln=Nd, Sm, Eu, Tb, Dy, and Yb. Calibration curves were made using Bi and Ln standards to find the relative concentration of Bi:Ln for each sample. In each synthesis, an excess of Ln was used, with a Bi:Ln ratio of approximately 9:1. The percentages of lanthanide incorporation into compounds **1** and **3** are given in Table 2. The given percentages reflect the maximum doping levels achieved and indicate that the bismuth environment is not favorable to lanthanide substitution.

Table 2 Percent Ln ion doping into each compound.

Compound	Ln Doping (mol%)
$Bi_{0.95}Nd_{0.05}$-1	3.8 ± 0.10
$Bi_{0.98}Sm_{0.02}$-1	1.9 ± 0.06
$Bi_{0.99}Eu_{0.01}$-1	0.5 ± 0.03
$Bi_{0.99}Tb_{0.01}$-1	0.7 ± 0.01
$Bi_{0.98}Dy_{0.02}$-1	1.9 ± 0.10
$Bi_{0.98}Yb_{0.02}$-1	2.0 ± 0.60
$Bi_{0.99}Eu_{0.01}$-3	0.3 ± 0.05

In the compounds reported here, doping is likely site-substitutional, as indicated by the single peak present in the $^5D_0 \rightarrow {}^7F_0$ transition for the Eu doped phases. Moreover, inspection of the crystal structures for **1** and **3** indicates a maximum void diameter of 3.4 Å and 3.6 Å, respectively. Given that a hydrated europium ion has a diameter of roughly 4.9 Å,[74] it is unlikely that that Eu incorporates into the interlayer spacing. Moreover, there is no apparent shift in the powder X-ray diffraction pattern as may be expected upon incorporation of the Ln^{3+} ion into the interlayer spacing suggesting the lanthanide ion is site-substituted within the bismuth framework (Fig. S6). To further confirm doping throughout the bismuth compound, luminescence data collected was collected for a single crystal of **$Bi_{0.99}Eu_{0.01}$-1** on a Raman spectrometer using a 405 nm excitation wavelength. The resulting emission showed distinct europium luminescence both along the length and depth of the crystal (e.g. on the crystal surface, 10 nm below the surface), supporting Ln doping throughout the crystals, and not solely limited to the surface (Fig. S38).

Photoluminescence

The solid-state luminescence of the reported compounds and their lanthanide-doped analogs was measured, and displayed metal-based emission in the visible region for the samarium, europium, terbium, and dysprosium analogs, and in the near-infrared for the neodymium, samarium, and ytterbium phases. The luminescence spectra of the free ligand, H_2TDC, was collected, giving an excitation maximum of 333 nm with subsequent emission at 353 nm (Fig. S25). The bismuth-only phase, **1**, exhibited distinct blue luminescence when excited with UV radiation, with maximum emission at 446 nm (Fig. 13a). Furthermore, a very short fluorescence lifetime (6.4(3) μs) was observed (Fig. S31). While there is precedent for emission in bismuth-organic compounds[24-27, 29, 31-39]; assignment of the emissive pathway can be challenging due to the variety of potential electronic transitions. Luminescence may be attributed to either metal-ligand or

ligand-metal charge-transfer, intraligand luminescence (n ← π*)/(π ← π*) that, in this case, is sufficiently red-shifted from the ligand emission, or additionally, metal centered emission from the Bi^{3+} ion itself from $^1P_1 \rightarrow {}^1S_0$ or $^3P_1 \rightarrow {}^1S_0$ transitions.[24-27, 29, 31-39]

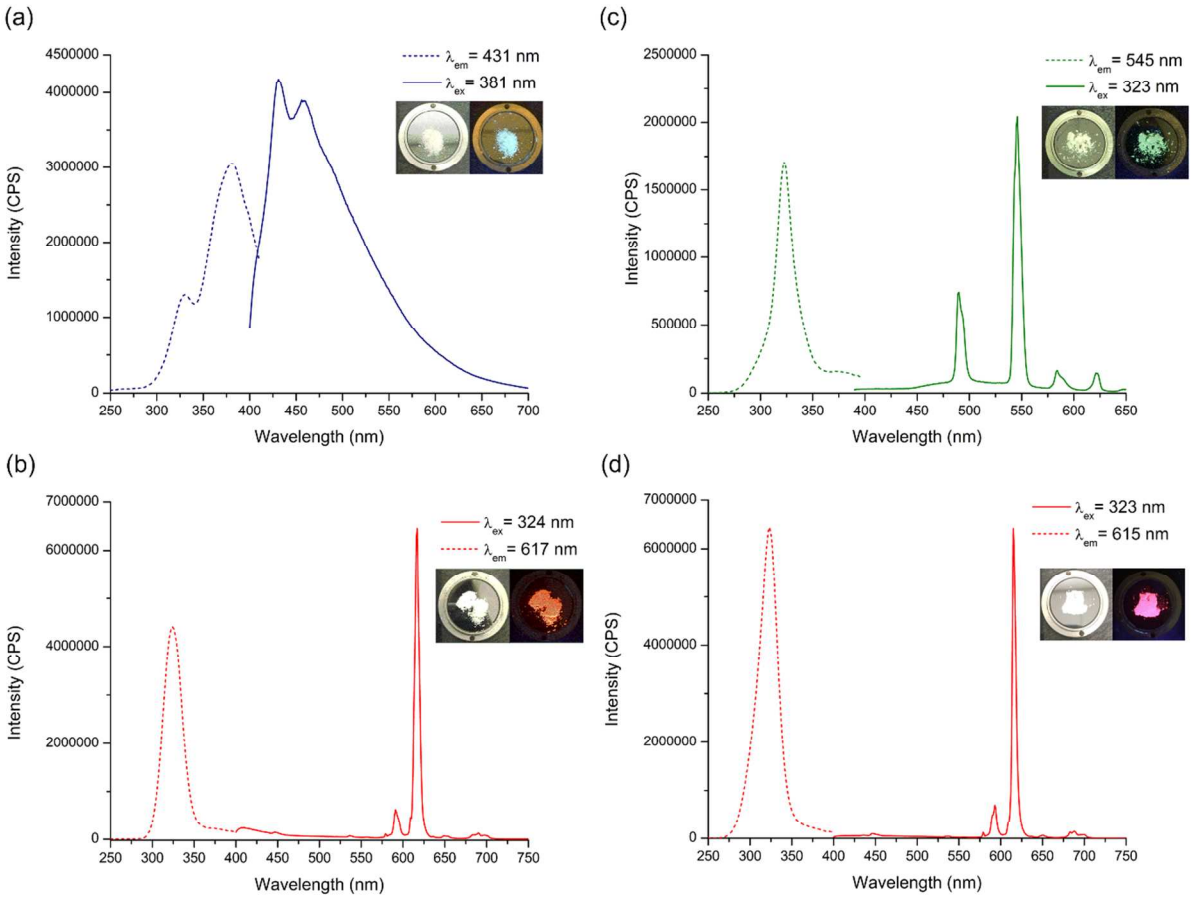

Fig. 13 Excitation (dashed line) and emission (solid line) spectra for (a) **1**, (b) **$Bi_{0.99}Eu_{0.01}$-1**, (c) **$Bi_{0.99}Tb_{0.01}$-1**, and (d) **$Bi_{0.99}Eu_{0.01}$-3**. Insets depict the bulk powder under ambient light (left) and UV radiation from a handheld lamp (right).

Upon doping with europium, characteristic red emission resulting from the 4*f*-4*f* transitions present for europium(III) was seen for **$Bi_{0.99}Eu_{0.01}$-1** (Fig. 13b). Compound **$Bi_{0.99}Eu_{0.01}$-1** excites at a maximum excitation wavelength of 324 nm, with a dominant emission peak observed at 617 nm corresponding to the hypersensitive $^5D_0 \rightarrow {}^7F_2$ transition. Additional emission peaks occur at 579 and 591 nm and can be assigned to the $^5D_0 \rightarrow {}^7F_J$ (J=0 and 1) transitions, respectively.[75] Weak emission peaks centered at 651 and 690 nm are assigned to the $^5D_0 \rightarrow {}^7F_3$ and $^5D_0 \rightarrow {}^7F_4$ transitions, respectively. The lifetime was determined to be 354(4) μs (Fig. S32). The total quantum yield, φ_{tot}, was found to be only 0.016(2) (Table 4).

For **$Bi_{0.99}Tb_{0.01}$-1**, excitation is seen at 323 nm, which gives rise to expected green luminescence (Fig. 13c). The $^5D_4 \rightarrow {}^4F_6$ transition is seen at 490 nm, while the intense peak at 545 nm can be assigned to the $^5D_4 \rightarrow {}^4F_5$ transition. Furthermore, additional peaks are observed

at 584 and 622 nm, assigned to the $^5D_4 \rightarrow {}^4F_J$ (J = 4 and 3, respectively) transitions. Time-resolved measurements yielded a fluorescence lifetime with a biexponential decay of 102(1) μs and 38(4) μs (Fig. S35). Quantum yield measurements gave a value of 0.0064(23) (Table 4).

Weak visible emission was seen from **$Bi_{0.98}Dy_{0.02}$-1**, with peaks at 484 and 574 nm corresponding to the $^4F_{9/2} \rightarrow {}^6H_{15/2}$ and $^4F_{9/2} \rightarrow {}^6H_{13/2}$ transitions, respectively, and at 616 nm, attributed to emission from a higher energy excited state, namely the $^4I_{15/2} \rightarrow {}^6H_{11/2}$ transition (Fig. S16). Broad ligand emission from TDC is seen centered around 420 nm. Two very weak emission peaks are evident at 662 and 751, attributed to the $^4F_{9/2} \rightarrow {}^6H_{11/2}$ and $^4F_{9/2} \rightarrow {}^6H_{9/2}$ transitions, respectively. A short-lived biexponential fluorescence lifetime was measured at 16(1) μs and 6(1) μs (Fig. S36).

Characteristic Sm^{III} luminescence peaks are observed at 562, 597, 643, and 703 nm, corresponding to the $^4G_{5/2} \rightarrow {}^6H_J$ (J = 5/2, 7/2, 9/2, and 11/2, respectively) (Fig. 27). NIR emission bands for the $^4G_{5/2} \rightarrow {}^6F_{5/2}$ and $^4G_{5/2} \rightarrow {}^6F_{9/2}$ transitions are seen at 945 and 1165 nm, respectively. A weak feature at 1027 nm is consistent with the $^4G_{5/2} \rightarrow {}^6F_{9/2}$ transition. Additionally, broad ligand based emission from TDC is seen centered around 420 nm. The compound exhibited a short biexponential decay with visible lifetimes of 89(2) μs and 15(1) μs) (Fig. S37).

Aside from **$Bi_{0.98}Sm_{0.02}$-1**, only **$Bi_{0.95}Nd_{0.05}$-1** and **$Bi_{0.98}Yb_{0.02}$-1** displayed NIR emission, with no evident emission from erbium or praseodymium analogs. Characteristic emission peaks are observed for the **$Bi_{0.95}Nd_{0.05}$-1** compound (Fig. S18). The $^4F_{3/2} \rightarrow {}^4I_J$ (J = 11/2, and 13/2) transitions are seen at 1061 and 1335 nm, respectively. The $^4F_{3/2} \rightarrow {}^4I_{9/2}$ transition is seen split with peaks at 875 and 916. Weak emission is observed for the **$Bi_{0.98}Yb_{0.02}$-1** compound, with the $^2F_{5/2} \rightarrow {}^2F_{7/2}$ transition seen as a broad feature centered around 977 nm (Fig. S19).

Characteristic red Eu(III) emission is observed for **$Bi_{0.99}Eu_{0.01}$-3** (Fig. 13d). The excitation maximum was observed at 323 nm. The $^5D_0 \rightarrow {}^7F_J$ (J = 1−2) transitions are assigned to the emission peaks at 593 and 615 nm, respectively, with the $^5D_0 \rightarrow {}^7F_0$ transition at 579 nm. Broad, weak peaks centered around 650 and 688 nm can be assigned to the $^5D_0 \rightarrow {}^7F_3$ and $^5D_0 \rightarrow {}^7F_4$ transitions, respectively. The fluorescence lifetime was found to be 640(2) μs (Fig. S33). Furthermore, the quantum yield for **$Bi_{0.99}Eu_{0.01}$-3** was determined to be 0.033(2) (Table 4).

The europium-only phase, **5**, also displays characteristic red emission (Fig. S30) upon excitation at 319 nm. The $^5D_0 \rightarrow {}^7F_J$ (J = 0−2) transitions are observed at 580, 593, and 615 nm respectively, while the broad peaks centered at 651 and 699 nm can be assigned to the $^5D_0 \rightarrow {}^7F_3$ and $^5D_0 \rightarrow {}^7F_4$ transitions. Additionally, Eu^{3+} absorption peaks are also evident in the excitation spectrum, with the most intense peak at 394 nm arising from the $^5L_6 \leftarrow {}^7F_0$ transition.[76] The fluorescence lifetime was found to be 182(1) μs (Fig. S34). For compound **5**, the quantum yield was measured to be 0.013(1) (Table 4).

For each of the visible emitters, the Commission Internationale L'Eclairage (CIE) coordinates were determined (Fig. 14). The lanthanide phases exhibit characteristic line like emission depending on the respective ion with Eu^{III} displaying red emission, Tb^{III} green, and

Sm^{III} light purple. The dysprosium analog of **1** displayed mostly ligand based emission, most likely due to inefficient sensitization of the lanthanide metal center.

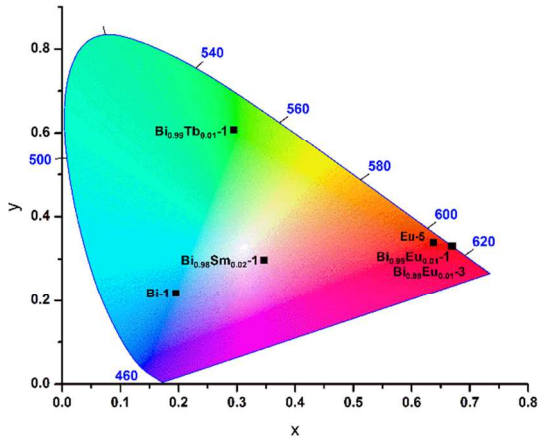

Fig. 14 CIE chromaticity coordinates of **1**, **5**, and Ln-doped phases with visible emission.

Discussion

The three bismuth compounds reported here consist of metal centers that adopt high coordination numbers (nine or ten), which is common for bismuth carboxylates.[17, 18] Furthermore, they each display significant asymmetry in their inner coordination sphere with Bi-O bond lengths as seen in Table 3. We attribute this asymmetry in part to the stereochemically active lone pair of the bismuth. Upon further inspection of the bismuth centers, distorted geometries with evident "open faces", which are *trans* to the shortest Bi-O bond distance are apparent. This is characteristic of an active $6s^2$ lone pair (Fig. 15). By comparison, the europium metal centers in **5** have much more isotropic coordination spheres. A cursory glance at the average metal-oxygen bond distances in **1**, **3**, **4**, and **5** (including O atoms from carboxylates and water molecules) shows relatively comparable average metal-oxygen bond distances (Table 3). However, closer inspection of these values indicates significant asymmetry of the Bi-O bond lengths from the chelating carboxylates that is not seen in the Eu-O carboxylate bond distances (Fig. 16a). This results in a greater distribution of the Bi-O bond lengths as compared to europium. This difference in the symmetry about the Bi and Eu metal centers is further highlighted by differences in the Bi-O bond distances from the carboxylate groups chelating the bismuth metal centers. For example, in **1**, the Bi1-O11 and Bi1-O12 bond lengths are 2.629(2) and 2.351(2) Å, respectively. In **5**, the Eu1-O13 and Eu1-O14 bond distances are 2.486(4) and 2.483(4) Å, respectively. Extending this comparison to include metal-O bond distances in all reported Bi-carboxylate and Eu-carboxylate compounds, a search through the Cambridge Structural Database[77] (Version 5.39) again gave rise to a similar bond distance distribution (Fig. 16 b,c). Here, the Bi-O distances have a much greater distribution from approximately 2.2 to 3.0 Å, while this range is notably smaller for the Eu-O distances.

Table 3 Metal-O bond distances for **1** and **3**-**5**.

	Average (Å)	Range (Å)
1 (Bi1)	2.528	2.351(2) – 2.685(2)
3 (Bi1)	2.559	2.360(4) – 2.737(4)[a]
4 (Eu1)	2.402	2.336(3) – 2.525(3)
5 (Eu1)	2.402	2.287(4) – 2.487(4)
5 (Eu2)	2.411	2.369(4) – 2.472(2)

[a]A long Bi-O interaction of 3.0359(3) Å is observed for **3**.

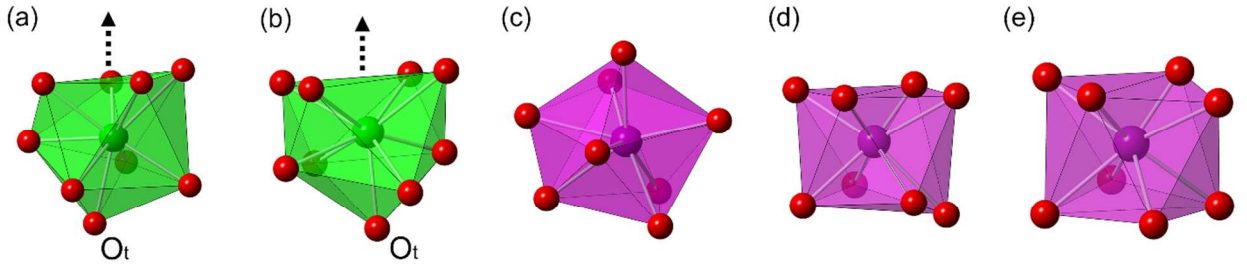

Fig. 15 Polyhedral representations of the metal center (a) Bi1 in **1**, (b) Bi1 in **3**, (c) Eu1 in **4**, (d) Eu1 in **5**, and (e) Eu2 in **5** with an arrow indicating possible direction of the stereochemically active lone pair on the bismuth metal center. The shortest Bi-O bond distance is labeled as O_t, trans to the proposed direction of the lone pair. The two unique bismuth centers in **2,** Bi1 and Bi2, are nearly identical to the bismuth centers in **1** and **3**, respectively**.** Noticeable distortion of the geometry about the metal center is seen in both bismuth polyhedra, whereas the europium centers for **5** each display square antiprism coordination environments and dodecahedron coordination for **4**. Bi=green polyhedra, Eu=purple polyhedra, O=red.

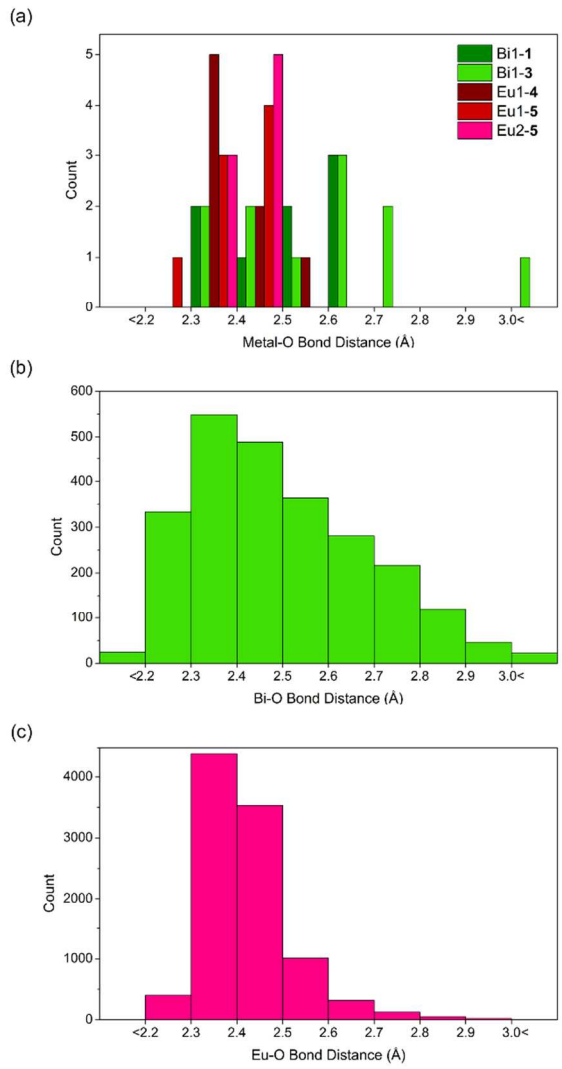

Fig. 16 Histograms displaying the range and frequency of metal-oxygen bond distances (a) in this work, (b) Bi-O bonds in all deposited Bi-carboxylates, and (c) Eu-O bonds in all deposited Eu-carboxylates. Bi-O and Eu-O bond distances for (b) and (c) were found using the Cambridge Structural Database Version 5.39,[77] updated November 2017; the metal-O bond distances were defined as a 3D parameter in ConQuest[78] and the resulting output was analyzed through Mercury.[78, 79] For sake of comparison, Bi1 and Bi2 in **2** were not included due to only a preliminary structure refinement being reported.

More than twenty unique lanthanide-TDC phases have been reported in addition to the ones described here and none are isostructural with the three Bi-TDC phases.[40-62] One bismuth-TDC phase has been presented previously in the literature, $[(CH_3)_2NH_2][Bi(TDC)_2]\cdot 1.5DMF$; however, this phase was isolated via solvothermal conditions using methanol and dimethylformamide (DMF).[29] By comparison, the compounds reported herein were isolated

under aqueous conditions, without the need of heat or organic solvents. Moreover, the structural diversity afforded by these compounds, particularly in the interlayer spacing highlights the diverse extended networks bismuth can afford upon slight variation of reaction conditions. Despite adopting similar topologies, the structures of **1-3** exhibit different interlayer interactions. In **1,** bound water molecules point into the interlayer, whereas in **2**, alternating water and terminal HTDC molecules point into the interlayer. By contrast, **3** displays only terminal HTDC molecules extending into the interlayer spacing.

Reacting europium nitrate with H_2TDC under identical synthetic conditions as that used to isolate **1** and **3**, yielded compounds **4** and **5**, which are distinctly different than the bismuth phases. These differences, attributed to difference in solubility and preferred coordination geometries, is likely responsible for the low doping levels observed in this work. The maximum doping achieved was less than 4% lanthanide incorporation. The inability to dope this compounds with greater amounts may, in part, be attributed to activity of the Bi^{3+} lone pair, wherein the anisotropy it might impart on the coordination geometry about the metal center is significant enough to lead to an unfavorable environment for the lanthanide ion, thereby limiting Ln incorporation.

As has been aforementioned, bismuth-organic materials can exhibit unique luminescence ranging from blue to green-yellow emission.[24-27, 29, 31-39] Cheetham et al. have reported blue emission from several bismuth-carboxylate compounds including [Bi(1,4-benezenedicarboxylate)$_2$]·dma and [LiBi(2,6-pyridinedicaboxylate)$_3$(H_2O)]·2dma, displaying broad emission peaks around 420 nm and 456 nm, respectively. This luminescence is similar to the broad blue emission of **1**, which they attribute to either charge transfer transitions or intraligand luminescence.[24, 25] Due to the nature of the transitions of the Eu^{3+} ion, analysis of the emission spectra for each of the europium doped bismuth phases (**$Bi_{0.99}Eu_{0.01}$-1** and **$Bi_{0.99}Eu_{0.01}$-3**) and **5** can help elucidate information regarding the possible environment about the metal center. In all three cases, presence of the $^5D_0 \rightarrow {}^7F_0$ transition indicates the Eu^{3+} ion is occupying a site in the lattice with either C_{nv}, C_n, or C_s symmetry.[75] Moreover, the relative intensity of the $^5D_0 \rightarrow {}^7F_2$ transitions in comparison to the weaker $^5D_0 \rightarrow {}^7F_1$ transitions are further consistent with low symmetry about the metal centers and the resulting red emission seen for each phase.[75]

The photophysical properties of these compounds were measured and are reported in Table 4. While it has not been determined to what extent the bismuth, the TDC ligands, or the pyridinium play in terms of sensitization, there is an evident difference in the luminescence efficiencies of **$Bi_{0.99}Eu_{0.01}$-1** and **$Bi_{0.99}Eu_{0.01}$-3** which could be attributed to the bound water molecule acting as a high-energy oscillator as well as the presence of an additional solvent water molecule in **$Bi_{0.99}Eu_{0.01}$-1**. While many Ln-TDC compounds have been reported, few report luminescence efficiency results for europium. Wang et al. reported two europium mixed ligand phases, [Emim][$(TDC)_2Eu_{1.5}$]$Cl_{1.25}Br_{0.25}$ and [Emim][$Eu(TDC)_2$], where Emim=1-methyl-3-ethylimidazolium, with quantum yields of 0.087 and 0.43, respectively, and lifetimes of 950 ms and 1030 μs, respectively.[47] Sun et al. reported lifetimes for [$Eu(TDC)(NO_3)(H_2O)]_n$ of 240 μs, although they did not give quantum yields.[46] Additionally, Heine et al. reported a biexponential

decay for the $^5D_0 \rightarrow {}^7F_2$ emission, with lifetimes of 547 and 723 μs for their Eu-doped bismuth-carboxylate MOF.[26] Our reported lifetimes are comparable these europium-TDC phases; however, the quantum yields and sensitization values for **1-3** are low by comparison, indicating the presented system is not as efficient as the Ln-TDC phases. The low quantum yield values could also be a result, in part, of the abundance of inner and outer coordination sphere water molecules and pyridinium cations, which are well-known luminescence quenchers. Efforts to remove such species are currently underway. Nonetheless the luminescence data is consistent with limited sensitization of the lanthanide ions via the Bi-TDC framework, which may be attributed in part to the TDC group and/or bismuth sensitization.

Table 4. Photophysical properties for the visible light emitters of **1**, **3**, **4**, and **5**.

	φ_{tot}	φ_{Eu}	lifetime (μs)	η_{sens}
$Bi_{0.99}Eu_{0.01}$-1	0.016(2)	0.172	354(4)	0.087
$Bi_{0.99}Tb_{0.01}$-1	0.0064(23)	-	102(1), 38(4)	-
$Bi_{0.99}Eu_{0.01}$-3	0.033(2)	0.297	640(2)	0.116
4	-	-	240[46]	-
5	0.013(1)	0.054	182(1)	0.252

Conclusions

Three bismuth(III)-thiophenedicarboxylate compounds were synthesized under aqueous, ambient conditions. similar synthetic techniques, both a previously reported and a new europium-thiophenedicarboxylate compound were isolated. The compounds were found to form either 2D sheets or 3D networks. The bismuth compounds adopted similar topologies yet exhibited different interlayer packing, arising from differences in the number of water and/or HTDC units pointing into the interlayer spacing. Lanthanide doping of the bismuth phases led to characteristic visible and NIR lanthanide based luminescence. While the lifetimes of the europium doped phases were consistent with other europium only compounds, the low quantum yields and sensitization efficiencies of the compounds point to the remove high energy oscillators such as pyridinium and water from the networks, potentially move to a more efficient sensitizing ligand system, and more generally, better understand the potential role of bismuth in the energy migration pathway. Nonetheless, these results into the structure-property relationships in Bi organic phases and their Ln doped analogs sheds new insight into the development of design strategies for the construction of bismuth-based frameworks as either intrinsically photoluminescent materials or platforms for harnessing the luminescent properties of other metal centers through doping.

Notes

The manuscript was written through contributions of all authors. All authors have given their approval to the final version of the manuscript.

Conflicts of interest

There are no conflicts to declare.

Acknowledgments

The authors gratefully acknowledge the Clare Booth Luce Foundation for their support. The authors also acknowledge the National Science Foundation for acquisition of the single crystal X-ray diffractometer (NSF CHE-1337975) and the Raman spectrometer (NSF CHE-1429079), as well as funding for BG (NSF CHE-REU 1156788).

Corresponding Author
*E-mail: kek44@georgetown.edu (KEK)

ORCID
Alyssa K. Adcock: 0000-0001-9977-3756
Bradley Gibbons: 0000-0003-2699-3621
Jeffrey D. Einkauf: 0000-0002-6403-4301
Jeffery A. Bertke: 0000-0002-3419-5163
J. Faye Rubinson: 0000-0002-4405-4348
Daniel T. de Lill: 0000-0003-0891-7246
Karah E. Knope: 0000-0002-5690-715X

References

1. K. Binnemans, *Chem. Rev.*, 2009, **109**, 4283-4374.
2. J.-C. G. Bunzli and C. Piguet, *Chem. Soc. Rev.*, 2005, **34**, 1048-1077.
3. S. V. Eliseeva and J.-C. G. Bunzli, *Chem. Soc. Rev.*, 2010, **39**, 189-227.
4. J.-C. G. Bünzli, *J. Coord. Chem.*, 2014, **67**, 3706-3733.
5. H. Dong, S.-R. Du, X.-Y. Zheng, G.-M. Lyu, L.-D. Sun, L.-D. Li, P.-Z. Zhang, C. Zhang and C.-H. Yan, *Chem. Rev.*, 2015, **115**, 10725-10815.
6. J.-C. G. Bünzli, *Chem. Rev.*, 2010, **110**, 2729-2755.
7. K. Kuriki, Y. Koike and Y. Okamoto, *Chem. Rev.*, 2002, **102**, 2347-2356.
8. J. C. Andres, A.-S., in *The Rare Earth Elements*, ed. D. A. Atwood, John Wiley & Sons Ltd, United Kingdom, 2012.
9. J.-C. G. E. Bünzli, S. V. , in *In Lanthanide Luminescence: Photophysical, Analytical and Biological Aspects*, ed. P. H. Hänninen, H, Springer, Berlin, Heidelberg, 2011.
10. A. Scarangella, R. Reitano, G. Franzò, F. Priolo and M. Miritello, *Appl. Phys. Lett.*, 2015, **107**, 041908.
11. P. Zhiwu, S. Qiang and Z. Jiyu, *Solid State Commun.*, 1993, **86**, 377-380.
12. J. Zhong, W. Zhao, E. Song and Y. Deng, *Journal of Luminescence*, 2014, **154**, 204-210.
13. K. Keshavamurthy and B. Eraiah, *Can. J. Phys.*, 2015, DOI: 10.1139/cjp-2015-0333.
14. *Critical Materials Strategy*, U. S. D. o. Energy, 2011.
15. G. G. Briand and N. Burford, *Chem. Rev.*, 1999, **99**, 2601-2658.
16. N. Yang and H. Sun, *Coord. Chem. Rev.*, 2007, **251**, 2354-2366.
17. M. Mehring, *Coord. Chem. Rev.*, 2007, **251**, 974-1006.
18. V. Stavila, R. L. Davidovich, A. Gulea and K. H. Whitmire, *Coord. Chem. Rev.*, 2006, **250**, 2782-2810.
19. J. Tang, Z. Zou and J. Ye, *Catal. Lett.*, 2004, **92**, 53-56.
20. S. Roggan, C. Limberg, M. Brandt and B. Ziemer, *J. Organomet. Chem.*, 2005, **690**, 5282-5289.
21. C. Liao, Z. Ma, G. Dong and J. Qiu, *Appl. Surf. Sci.*, 2014, **314**, 481-489.
22. D. Wu, T. He, J. Xia and Y. Tan, *Mater. Lett.*, 2015, **156**, 195-197.
23. J. Wu, H. Zhang and S. Du, *J. Mater. Chem. C*, 2016, **4**, 3364-3374.
24. A. Thirumurugan and A. K. Cheetham, *Eur. J. Inorg. Chem.*, 2010, **2010**, 3823-3828.
25. A. Thirumurugan, W. Li and A. K. Cheetham, *Dalton Trans.*, 2012, **41**, 4126-4134.
26. J. Heine, T. Wehner, R. Bertermann, A. Steffen and K. Müller-Buschbaum, *Inorg. Chem.*, 2014, **53**, 7197-7203.
27. M. Feyand, M. Köppen, G. Friedrichs and N. Stock, *Chem. Eur. J.*, 2013, **19**, 12537-12546.
28. R. J. Batrice, R. L. Ayscue, A. K. Adcock, B. R. Sullivan, S. Y. Han, P. M. Piccoli, J. A. Bertke and K. E. Knope, *Chem. Eur. J.*, 2018, **24**, 5630-5636.
29. L. Kan, J. Li, X. Luo, G. Li and Y. Liu, *Inorg. Chem. Commun.*, 2017, **85**, 70-73.
30. R. Shannon, *Acta Crystallogr., Sect. A*, 1976, **32**, 751-767.
31. A. C. Wibowo, S. A. Vaughn, M. D. Smith and H.-C. zur Loye, *Inorg. Chem.*, 2010, **49**, 11001-11008.
32. A. C. Wibowo, M. D. Smith and H.-C. zur Loye, *Cryst. Growth Des.*, 2011, **11**, 4449-4457.
33. A. C. Wibowo, M. D. Smith and H.-C. zur Loye, *Chem. Commun.*, 2011, **47**, 7371-7373.
34. J. R. Sorg, T. Wehner, P. Matthes, R. Sure, S. Grimme, J. Heine and K. Muller-Buschbaum, *Dalton Trans.*, 2018, DOI: 10.1039/C8DT00642C.
35. X.-P. Zhang, H.-R. Tian, G.-F. Yan, Y. Su, Y.-L. Feng and J.-W. Cheng, *Dalton Trans.*, 2013, **42**, 1088-1093.

36. X.-P. Zhang, D.-G. Wang, Y. Su, H.-R. Tian, J.-J. Lin, Y.-L. Feng and J.-W. Cheng, *Dalton Trans.*, 2013, **42**, 10384-10387.
37. N. Shen, J. Li, Z. Wu, B. Hu, C. Cheng, Z. Wang, L. Gong and X. Huang, *Chem. Eur. J.*, 2017, **23**, 15795-15804.
38. O. Toma, N. Mercier and C. Botta, *Eur. J. Inorg. Chem.*, 2013, **2013**, 1113-1117.
39. X. Yu, H. Zhang, Y. Cao, Z. Hu, Y. Chen and Z. Wang, *J. Solid State Chem.*, 2006, **179**, 3095-3100.
40. B.-L. Chen, K.-F. Mok, S.-C. Ng and M. G. B. Drew, *New J. Chem.*, 1999, **23**, 877-883.
41. L. F. Marques, M. V. dos Santos, S. J. L. Ribeiro, E. E. Castellano and F. C. Machado, *Polyhedron*, 2012, **38**, 149-156.
42. J.-G. Wang, C.-C. Huang, X.-H. Huang and D.-S. Liu, *Cryst. Growth Des.*, 2008, **8**, 795-798.
43. Z. Chen, B. Zhao, P. Cheng, X.-Q. Zhao, W. Shi and Y. Song, *Inorg. Chem.*, 2009, **48**, 3493-3495.
44. W. Huang, D. Wu, P. Zhou, W. Yan, D. Guo, C. Duan and Q. Meng, *Cryst. Growth Des.*, 2009, **9**, 1361-1369.
45. C. MacNeill, C. Day, S. Gamboa, A. Lachgar and R. Noftle, *J. Chem. Crystallogr.*, 2010, **40**, 222-230.
46. Y.-g. Sun, B. Jiang, T.-f. Cui, G. Xiong, P. F. Smet, F. Ding, E.-j. Gao, T.-y. Lv, K. Van den Eeckhout, D. Poelman and F. Verpoort, *Dalton Trans.*, 2011, **40**, 11581-11590.
47. M.-X. Wang, L.-S. Long, R.-B. Huang and L.-S. Zheng, *Chem. Commun.*, 2011, **47**, 9834-9836.
48. J. Xu, J. Cheng, W. Su and M. Hong, *Cryst. Growth Des.*, 2011, **11**, 2294-2301.
49. X.-G. Du, J. Zhang and J.-J. Li, *Acta Crystallogr. Sect. E: Struct. Rep. Online*, 2012, **68**, m1024.
50. J. Ren, Y. Liu, Z. Chen, G. Xiong and B. Zhao, *Sci. China Chem.*, 2012, **55**, 1073-1078.
51. J.-J. Wang, L.-P. Zhang, L. Huang and J. Chen, *J. Coord. Chem.*, 2012, **65**, 3274-3286.
52. P. J. Calderone, A. M. Plonka, D. Banerjee, Q. A. Nizami and J. B. Parise, *Solid State Sciences*, 2013, **15**, 36-41.
53. L. F. Marques, C. C. Corrêa, R. R. da Silva, M. V. dos Santos, S. J. L. Ribeiro and F. C. Machado, *Inorg. Chem. Commun.*, 2013, **37**, 66-70.
54. C.-S. Tsai, W.-T. Chen and J.-H. Liao, *J. Chin. Chem. Soc.*, 2013, **60**, 755-761.
55. K. P. Carter, C. H. F. Zulato, E. M. Rodrigues, S. J. A. Pope, F. A. Sigoli and C. L. Cahill, *Dalton Trans.*, 2015, **44**, 15843-15854.
56. N. L. Rosi, J. Kim, M. Eddaoudi, B. Chen, M. O'Keeffe and O. M. Yaghi, *J. Am. Chem. Soc.*, 2005, **127**, 1504-1518.
57. C.-H. Zhan, F. Wang, Y. Kang and J. Zhang, *Inorg. Chem.*, 2012, **51**, 523-530.
58. L. F. Marques, C. C. Correa, S. J. L. Ribeiro, M. V. dos Santos, J. D. L. Dutra, R. O. Freire and F. C. Machado, *J. Solid State Chem.*, 2015, **227**, 68-78.
59. L. F. Marques, A. A. B. Cantaruti Júnior, S. J. L. Ribeiro, F. M. Scaldini and F. C. Machado, *Opt. Mater.*, 2013, **35**, 2357-2365.
60. C.-L. Guo, X. Zhuo, Y.-Z. Li and H.-G. Zheng, *Inorg. Chem. Acta*, 2009, **362**, 491-501.
61. M. Fang, Z. Chen, G.-W. Yin, X.-M. Kang and H. Xu, *Inorg. Chem. Commun.*, 2016, **70**, 51-55.
62. Y. Zhao and S.-H. Li, *Synthesis and Reactivity in Inorganic, Metal-Organic, and Nano-Metal Chemistry*, 2015, **45**, 921-925.
63. *SAINT*, Bruker AXS Inc., Madison, WI, USA, 2007.
64. *APEX2*, Bruker AXS Inc., Madison, WI, USA, 2008.
65. *SADABS*, Bruker AXS Inc., Madison, WI, USA, 2008.
66. G. Sheldrick, *Acta Crystallogr., Sect. A*, 2008, **64**, 112-122.
67. L. J. Farraguia, *J. Appl. Cryst.*, 2012, **45**, 849-845.
68. O. Shigeru, F. Naomichi, W. Takao, O. Yoshio and H. Masayuki, *Bulletin of the Chemical Society of Japan*, 1965, **38**, 1247-1253.

69. P. M. Dewick, *Essentials of Organic Chemistry: For Students of Pharmacy, Medicinal Chemistry and Biological Chemistry*, John Wiley & Sons, 2006.
70. A. Spek, *Acta Crystallogr., Sect. D*, 2009, **65**, 148-155.
71. K. Nakamoto, *Part A: Theory and Applications in Inorganic Chemistry*, John Wiley & Sons, Inc. , Hoboken, New Jersey Sixth edn., 2009.
72. A. K. Adcock, R. J. Batrice, J. A. Bertke and K. E. Knope, *Eur. J. Inorg. Chem.*, 2017, **2017**, 1435-1445.
73. F. Cagnin, M. R. Davolos and E. E. Castellano, *Polyhedron*, 2014, **67**, 65-72.
74. S. Yang, G. Sheng, G. Montavon, Z. Guo, X. Tan, B. Grambow and X. Wang, *Geochim. Cosmochim. Acta*, 2013, **121**, 84-104.
75. K. Binnemans, *Coord. Chem. Rev.*, 2015, **295**, 1-45.
76. K. Binnemans and C. Görller-Walrand, *Chem. Phys. Lett.*, 1995, **235**, 163-174.
77. C. R. Groom, I. J. Bruno, M. P. Lightfoot and S. C. Ward, *Acta Crystallogr., Sect. B: Struct. Sci*, 2016, **72**, 171-179.
78. I. J. Bruno, J. C. Cole, P. R. Edgington, M. Kessler, C. F. Macrae, P. McCabe, J. Pearson and R. Taylor, *Acta Crystallogr., Sect. B: Struct. Sci*, 2002, **58**, 389-397.
79. C. F. Macrae, P. R. Edgington, P. McCabe, E. Pidcock, G. P. Shields, R. Taylor, M. Towler and J. van de Streek, *J. Appl. Crystallogr.*, 2006, **39**, 453-457.

Table of Contents Graphic: Bismuth(III) - Thiophenedicarboxylates as Host Frameworks for Lanthanide Ions: Synthesis, Structural Characterization, and Photoluminescence

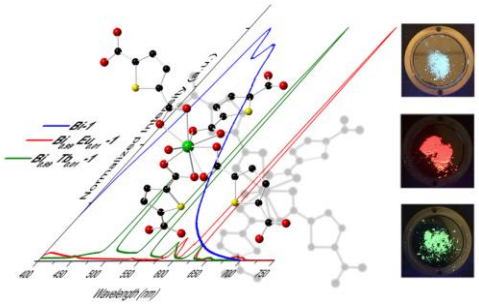

Three bismuth-thiophenedicarboxylate compounds, two of which were lanthanide-doped, and two europium- thiophenedicarboxylate phases were synthesized under aqueous conditions and characterized.